Metal-organic framework glass anode with an exceptional cycling-induced capacity enhancement for lithium-ion batteries

Gao, Chengwei; Zhang, Z.J.; Qi, S.B.; Wang, P.X.; Jensen, Lars Rosgaard; Johansen, M.; Christensen, C.K.; Zhang, Y.F.; Ravnsbæk, D.B.; Yue, Yuanzheng

Published in:
Advanced Materials

DOI (link to publication from Publisher):
10.1002/adma.202110048

Publication date:
2022

Document Version
Accepted author manuscript, peer reviewed version

Metal-organic framework glass anode with an exceptional cycling-induced capacity enhancement for lithium-ion batteries

Chengwei Gao, Zhenjing Jiang, Shibin Qi, Peixing Wang, Lars Rosgaard Jensen, Morten Johansen, Christian Kolle Christensen, Yanfei Zhang, Dorthe Bomholdt Ravnsbæk*, Yuanzheng Yue**

C. W. Gao, Y. Z. Yue
Department of Chemistry and Bioscience, Aalborg University, 9220 Aalborg, Denmark

E-mail: yy@bio.aau.dk

C. W. Gao

Laboratory of Infrared Material and Devices, Advanced Technology Research Institute, Ningbo University, Ningbo, 315211, China

C. W. Gao, Z. J. Jiang, S. B. Qi, P. X. Wang, Y. F. Zhang

School of Materials Science and Engineering, Qilu University of Technology (Shandong Academy of Science), Jinan 250353, China
E-mail: zhang-yanfei@hotmail.com

L. R. Jensen

Department of Materials and Production, Aalborg University, 9220 Aalborg, Denmark

M. Johansen, C. K. Christensen

Department of Physics, Chemistry and Pharmacy, University of Southern Denmark, 5230 Odense M, Denmark

D. B. Ravnsbæk

Department of Chemistry, Aarhus University, 8000 Aarhus C, Denmark

This article has been accepted for publication and undergone full peer review but has not been through the copyediting, typesetting, pagination and proofreading process, which may lead to differences between this version and the Version of Record. Please cite this article as doi: 10.1002/adma.202110048.

E-mail: dorthe@chem.au.dk

Keywords: Lithium-ion batteries; Anode; Metal-organic framework crystal; Metal-organic framework glass; Capacity enhancement

Abstract

Metal organic frameworks (MOFs) hold great promise as high-energy anode materials for next-generation lithium-ion batteries (LIBs) due to their tunable chemistry, pore structure and abundant reaction sites. However, the pore structure of crystalline MOFs tends to collapse during lithium-ion insertion and extraction, and hence, their electrochemical performances are rather limited. As a critical breakthrough, a MOF glass anode for LIBs has been developed in the present work. In detail, it was fabricated by melt-quenching Cobalt-ZIF-62 ($Co(Im)_{1.75}(bIm)_{0.25}$) to glass, and then by combining glass with carbon black and binder. The derived anode exhibits high lithium storage capacity (306 mAh g^{-1} after 1000 cycles at of 2 A g^{-1}), outstanding cycling stability and superior rate performance compared with the crystalline Cobalt-ZIF-62 and the amorphous one prepared by high-energy ball-milling. Importantly, it was found that the Li-ion storage capacity of the MOF glass anode continuously rises with charge-discharge cycling and even *tripled* after 1000 cycles. Combined spectroscopic and structural analyses, along with density functional theory calculations, revealed the origin of the unusual cycling-enhancement of the performances of the MOF glass anode, that is, increased distortion and local breakage of the Co-N coordination making the Li-ion intercalation sites more accessible.

1. Introduction

Confronting the gradual depletion of fossil energy and the subsequent environmental degradation, it is the utmost urgency to develop advanced sustainable energy storage and conversion systems. To date, lithium-ion batteries (LIBs), as one of the vital energy storage devices, still dominate the commercial markets. However, large-scale energy storage devices and hybrid electric vehicles demand breakthroughs in enhancing the power/energy density, safety and cycling life of the LIBs. In this context, extensive research is being conducted to seek new anode materials with superior lithium storage performance.[1–3]

Metal organic frameworks (MOFs), assembled by metal ions and organic ligands, are considered to be one of the most promising anode candidates for high-performance LIBs owing to their great porosity, abundant reaction sites and tunable structures.[4–6] The polycrystalline MOF-177 was first applied as the anode material for LIBs, delivering a high initial irreversible capacity of 400 mAh g^{-1}. However, the capacity rapidly decayed to 105 mAh g^{-1} after only two cycles.[7] Although some MOFs are promising anode materials of LIBs, poor cycling stability due to destruction of the framework is still a big challenge to be overcome. The structural collapse in most of MOFs anodes was found to be caused by the interactions between the metal-ligand coordination bonds in MOFs and lithium ions during cycling processes.[7] Moreover, MOFs face another significant challenge of poor electronic conductivity for electrochemical applications. To overcome these challenges and to improve the electrochemical properties, pure MOFs are generally used as hosts of metal oxide nanoparticles to prepare composites, or as templates/precursors to synthesize MOFs derivatives such as porous carbons and carbon composites.[8–10] However, these processes are usually realized at the expense of destroying the intrinsic organic-inorganic hybrid structures of MOFs. Therefore, it is critically important to ensure the structure integrity of MOFs for maintaining both the active surface area and the electronic conductivity in LIB anodes during operation.

To this end, the order/disorder engineering concept was proposed to enhance the electrochemical performances of Al-MOF/graphene composite anode for LIBs.[11] Specifically, the partial disordering in the Al-MOF particles induced by the lithiation/delithiation process enabled efficient lithium storage and cycling stability enhancement owing to the reduced Li^+ ion diffusion distance and the opened structure to buffer the mechanical stresses. Besides the order-disorder transition during the lithiation/delithiation process, the amorphization of polycrystalline MOFs can also be achieved via many other different routes, e.g., mechanosynthesis,[12] mechanical milling,[13] thermal[14] and pressure treatment.[15] In terms of the microstructure, the mechanically amorphized MOFs inherit some of the crystal characteristics, e.g., the short- and medium-range order, framework

connectivity, and porosity, while both long-range disorder and defects can be induced during the mechanical milling process.[15] In addition to mechanically amorphized MOFs, another class of disordered MOFs, MOF glass, emerged six years ago.[16] As a sub-class of MOFs, some of ZIFs can be melted before decomposition at high temperature and then quenched to glass state, i.e., the so-called melt-quenched (MQ) metal organic framework (MOF) glasses.[16,17] This new family of glass materials possesses intriguing structural and chemical characteristics, which grand them distinct thermal, mechanic, dynamic properties. For instance, ZIF-4 MQ glass possesses a higher thermal conductivity than their crystalline counterparts.[18] The ZIF-62 MQ glass exhibits the highest glass forming ability in all known glass materials and shear banding under indentation.[19,20] The microstructure of MQ-ZIF glasses are rather different from those of their counterparts: crystalline ZIFs and mechanically amorphized ZIFs, e.g., in short range disorder, defect concentration and pore structure. Very recently, the direct evidence for a high degree of short-range disorder in ZIF glasses were discovered with ultrahigh-field Zn^{67} solid-state nuclear magnetic resonance spectroscopy.[21] The short-range disorder arises from the lower rigidity and larger size of the tetrahedral units in comparison to inorganic network glasses that possess short-range order structure. In addition, since the chemical component of parent crystalline MOF could be tuned, MOF glass with different components can be readily prepared via the melt-quenching method. These distinct features provide a unique opportunity to investigate whether MQ-ZIF glasses could be utilized as superior anode materials in LIBs, since they could be beneficial to the lithium-ion transfer kinetics. This work is the first attempt to find out which ZIF structure has the greatest potential to be used for fabricating high-performance LIB anode, i.e., among melt-quenched structure, mechanically amorphized structure and crystalline structure.

The crystalline ZIF-62 is constructed by the metal nodes (cobalt) and organic ligands such as imidazolate (Im) and benzimidazolate (bIm), which is expressed by the chemical formula $Co[Im_{1.75}bIm_{0.25}]$. The nodes and the linkers are connected by coordination bonds that are much

weaker than covalent bonds inside the linkers. It has been found that Cobalt-ZIF-62 can be melt-quenched to the glass state.[22] Moreover, it has been confirmed that the pores in Cobalt-ZIF-62 crystal can be partly retained in its glass state upon melt-quenching, and hence, Cobalt-ZIF-62 glass is regarded as an excellent material for gas separation and storage.[22,23]

By taking advantage of the nano porous structure of MQ Cobalt-ZIF-62 glass (ZIF glass), in this work the LIB anodes were fabricated from this glass and characterized electrochemical performances. In parallel, both the crystalline and the mechanically amorphized Cobalt-ZIF-62 anodes were also prepared, which are denoted as ZIF crystal and amorphous ZIF for simplicity. Then a detailed comparison was made among the three types of anodes concerning their cycling performance and structural evolution. Remarkably, the ZIF glass anode exhibits unusual electrochemical performances, and in particular, 200% enhancement of the capacity caused by 1000 discharging/charging cycles at a high current density of 2 A g^{-1}.

2. Fabrication and Material Characteristics

Figure 1a schematically shows the preparation of the ZIF crystal, ZIF glass and amorphous ZIF, and the final anode for LIBs. ZIF crystal was synthesized by a solvothermal method with slight modifications.[24] ZIF glass was obtained by quenching ZIF melt to room temperature and amorphous ZIF was produced by subjecting ZIF crystal to a high-energy ball milling process. ZIF glass presents similar bulk particles to ZIF crystal as seen in SEM and TEM images in Figures 1b and S1-S3. The average particle size of the amorphous ZIF is much smaller than that of ZIF crystal since the amorphous ZIF is finely ground during ball milling. As shown in Figure 1c, the powder X-ray diffraction (PXRD) pattern of the as-prepared ZIF crystal resembles that of the simulated pattern (CCDC No. 671070), confirming the successful synthesis of the ZIF-62 crystal.[24] Upon either melt-quenching or ball milling, all the diffraction peaks assigned to ZIF crystal disappear, indicating that

the ZIF structure becomes disordered.[16] Analysis of the Pair distribution Functions (PDF) obtained from total X-ray scattering data reveals that the local atomic structure of the three ZIF materials are highly similar and can all be fitted using the model for the crystal structure of Co ZIF-62 (CCDC No. 671070) as shown by the comparison between the observed and simulated data in Figure 1d. The fits and parameters resulting from the PDF analysis are shown in Figures S4 and Table S1. Hence, the PDF analysis confirms that both the building blocks and the framework of the Co ZIF-62 structure is intact after the melt-quenching or ball milling process.

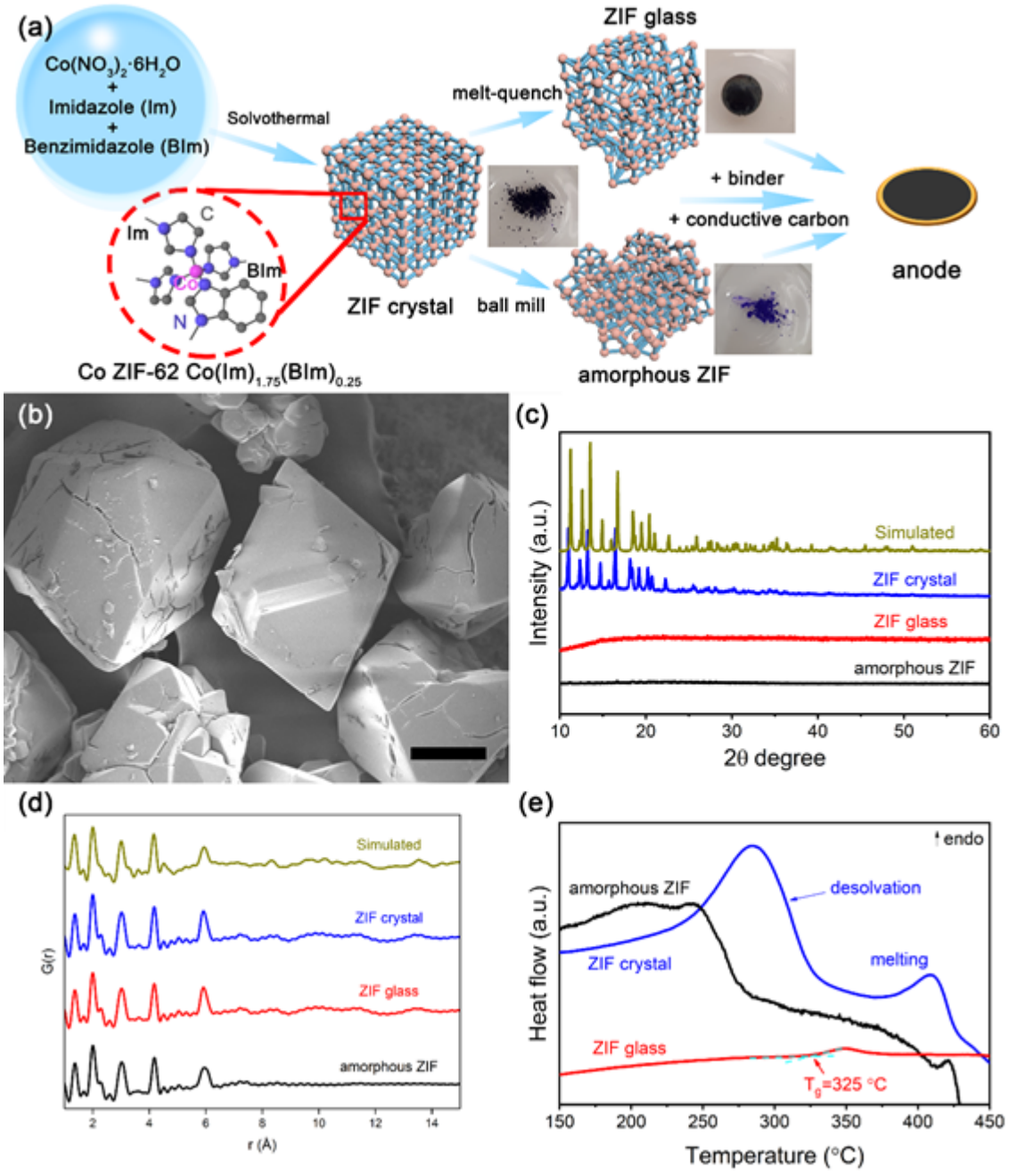

Figure 1. Schematic illustration and structural characterizations of ZIF crystal, glass and amorphous ZIF. (a) Preparation of ZIF crystal (Co ZIF-62, $Co(Im)_{1.75}(BIm)_{0.25}$), ZIF glass and amorphous ZIF by hydrothermal, melt-quenching and ball milling methods, respectively. The schematic representation of the structure of Co ZIF-62 (hydrogen atoms omitted for simplicity). Fabrication of anode: Mixing the ZIF materials with carbon black and binder, and pasting the mixture onto a copper foil substrate. (b) SEM image of ZIF glass with a scale bar of 100 μm. (c) X-ray diffraction patterns showing the loss

of long-range order in ZIF crystal after the melt-quenching or ball milling process. (d) Pair distribution functions (PDFs) obtained from total X-ray scattering showing the similarity of the local atomic structure of the three ZIF samples to each other and to the crystal structure of Co ZIF-62 (simulated). (e) The differential scanning calorimetry (DSC) upscan curves of three ZIF samples in argon atmosphere at 10°C min^{-1}.

Evidently, long range order is completely lost in the glassy and amorphous ZIF as no well-defined interatomic correlations are observed at r > 6.2 Å in the PDFs, which gives rise to refined coherent domain sizes (sp-diameters) of 15-20 Å for the glassy and amorphous ZIF. In contrast, the crystalline ZIF has a coherent domain size of >100 Å. We also note that the isotropic thermal vibration of Co at distances >4.7 Å is ~17 times larger in the amorphous ZIF than compared to the glassy ZIF. This point confirms a significantly higher degree of lattice order in the glassy ZIF compared to the amorphous ZIF. Furthermore, the subtle structural differences between ZIF glass and amorphous ZIF were also revealed by the differential scanning calorimetry (DSC). As shown in Figure 1e, during a DSC upscan at 10 °C min^{-1}, the as-prepared ZIF crystal undergoes solvent release corresponding to the endothermic peak at 270 °C, and subsequent melting that causes the endothermic peak at around 435 °C. During the heating process of the glass, a glass transition peak is observed, which is a typical feature of a melt-quenched glass. The onset temperature of the peak is defined as the standard glass transition temperature (T_g),[25] which is 325 °C for the studied ZIF glass. In Figure 1e, amorphous ZIF exhibits two endothermic events (desolvation and melting) during DSC upscan, similarly to ZIF crystal. However, the former shows less enthalpy gain for both desolvation and melting, lower desolvation peak temperature and slightly higher melting peak temperature. To evaluate the thermal stability, thermogravimetry (TG) curves of the three samples were collected (Figure S5a). Significant mass losses are observed in TG curves from 100 to 300 °C for both the ZIF crystal and

amorphous ZIF owing to the solvent release while nearly no mass loss is observed for ZIF glass since the solvent was already released during the glass preparation process. Moreover, the onset temperature of the mass loss in amorphous ZIF is lower than that in ZIF crystal. This implies that DMF molecules are easier to be released from amorphous ZIF due to its broken framework than from ZIF crystal.

The Fourier-transform infrared spectroscopy (FTIR) spectra of the three ZIF samples are shown in **Figure 2**a. Besides the peak at around 430 cm^{-1} related to Co-N exists in the spectra of the three ZIF samples, an extra peak at around 425 cm^{-1} was observed in the spectra of ZIF glass and amorphous ZIF, respectively (see the inset of Figure 2a). This new peak might arise from the new groups of Co-N specimens, which were introduced during the melt-quenching or ball milling process. The lower wave number of the new peak position implies the weaker bonds of these new groups, suggesting that these newly formed Co-N bonds in ZIF glass and amorphous ZIF are more vulnerable to the lithiation/delithiation than those in ZIF crystal. The peaks at 1676 cm^{-1} in the spectra of both ZIF crystal and amorphous ZIF are associated with the vibrational mode of the carbonyl groups of solvent molecules (DMF) trapped in pores of ZIFs. There is no detectable peak at 1676 cm^{-1} in the spectrum of ZIF glass, indicating that the DMF molecules escaped from the sample during the heating process. This agrees well with the thermogravimetric analysis (Figure S5a). In addition, the peaks at 1465, 1235, 1082, 668 cm^{-1} can be observed in the spectra of all three samples, which correspond to C-N stretching, C-H in-plane-bending, C-H out-of-plane-bending and ring deformation out-of-plane-bending in the organic ligands, respectively.[26] Figure 2b shows the Raman spectra of the three ZIF samples, which share the similar peaks in the range of 200~1100 cm^{-1} with a sharp peak at around 680 cm^{-1}. This implies the well-preserved organic ligands in ZIF glass and amorphous ZIF. However, the sharp peak at 1160 cm^{-1} in the spectrum of ZIF crystal becomes considerably broader and weaker upon either mechanical amorphization or melt-quenching (see also Figure S5b). This could be attributed to the distortion of C-N bond breakage caused by the mechanic amorphization

and vitrification processes.[19,27,28] In short, both the Raman and FTIR spectra confirm that the integrity of organic ligands is preserved in the three samples after the melt-quenching or ball milling process.

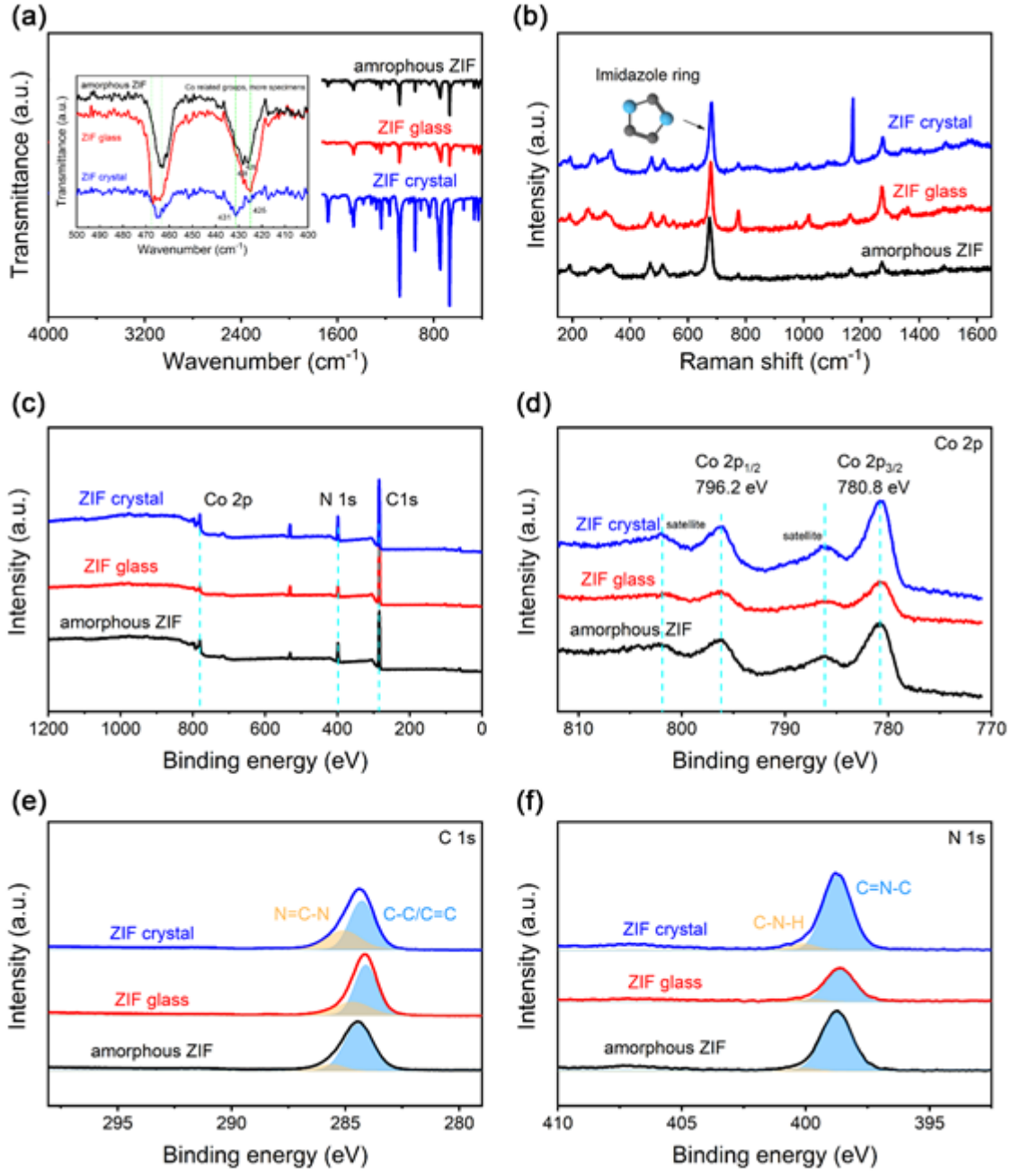

Figure 2. Spectroscopic characterization of the ZIF crystal, ZIF glass and amorphous ZIF. (a) Fourier-transform infrared spectroscopy (FTIR) spectra of three ZIF samples (Inset: High-resolution spectra from 500 to 400 cm^{-1} of three ZIF samples). (b) Raman spectra with the range from 150 to 1650 cm^{-1}

of all three ZIF samples. XPS survey spectra (c), high resolution spectra of Co 2p (d), C 1s (e), and N 1s (f), demonstrating that these three samples consist of same composition.

X-ray photoelectron spectroscopy (XPS) spectra were collected to reveal the surface chemistry of the three ZIF samples. From the survey spectra in Figure 2c, the elements (Co, C and N) involved in the three samples can be detected. Figure 2d shows the core level spectra of Co 2p, in which the Co $2p_{1/2}$ and Co $2p_{3/2}$ peaks locate at 796.2 and 780.8 eV with two satellite peaks at 801.9 and 786.2 eV, respectively. The three samples exhibit the same peaks of Co 2p, implying that the majority of Co exists as Co^{2+}, which remains unaffected during the melt-quenching or ball milling process.[29] In Figure 2e, the peak of C 1s for each sample can be deconvoluted into two peaks assigned to C-C/C=C at 284.2 eV and N=C-N at 286 eV, respectively.[30] In the N 1s core level XPS spectrum (Figure 2f), the peaks at 398.7 and 399.5 eV arises from the bonds of C=N-C and C-N-H, respectively.[30] It is evident that the three samples present almost identical C 1s and N 1s spectra, suggesting that both the melt-quenching and ball milling pose little impact on the imidazole and benzimidazole ligands in ZIFs. As shown in Figure S6, the average pore sizes of ZIF crystal, ZIF glass and amorphous ZIF from N_2 adsorption-desorption isotherms are found to be 3.4, 4.3 and 3.8 nm, respectively. The CO_2 sorption of ZIF crystal is a type I isotherm with a capacity of about 1 mmol g^{-1} CO_2 at 95kPa, which is consistent with previous reports.[22] From the above-presented results, it is confirmed that both the melt-quenching and the ball milling processes did not affect the chemical composition of Cobalt-ZIF-62 but made its microstructure highly disordered. Then, how the disorder of the ZIF structure impacts were investigated on the electrochemical performances of the ZIF based anode for LIBs.

3. Electrochemical Performances

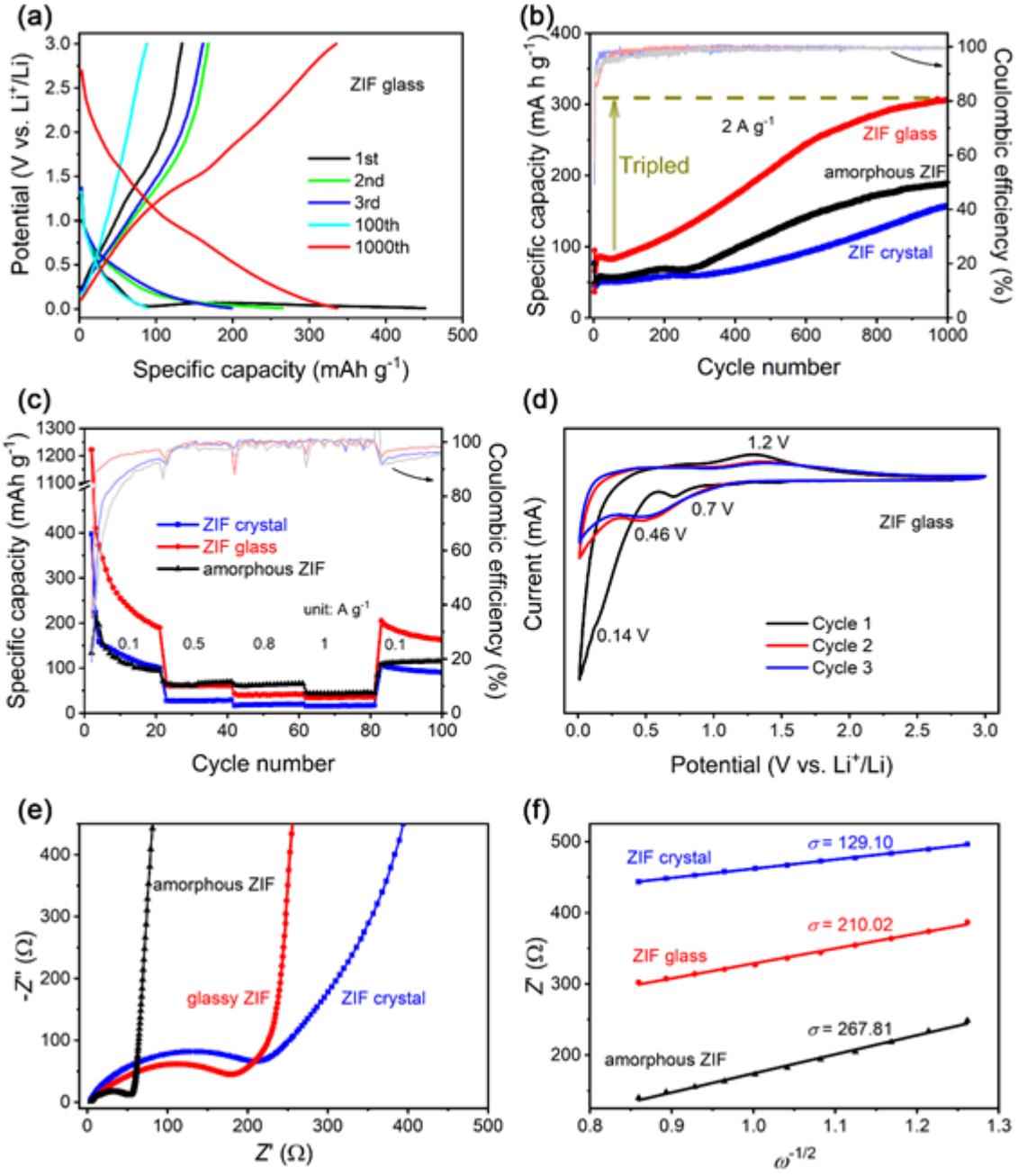

Figure 3. Electrochemical properties of ZIF crystal, ZIF glass and amorphous ZIF. (a) Galvanostatic charge-discharge profiles of ZIF glass for different cycles at the current density of 1 A g^{-1}. (b) The cycling performance of ZIF crystal, ZIF glass and amorphous ZIF at 2 A g^{-1} for 1000 cycles. (c) Rate performance of the three samples at current densities of 0.1, 0.5, 0.8, 1 and 0.1A g^{-1} for 20 cycles. (d) Cyclic Voltammetry (CV) curves of ZIF glass within the range from 0.01 to 3.0 V at a scan rate of 0.1 mV s^{-1}. (e) Nyquist plots obtained from electrochemical impedance spectra within frequency range

from 0.01 to 100 kHz with an amplitude of 10 mV. (f) Z' vs. $\omega^{-1/2}$ plots in the low frequency region obtained from Nyquist plots.

The electrochemical performances of the anodes made from the ZIF crystal, ZIF glass and amorphous ZIF, respectively, are characterized by galvanostatic charge/discharge cycling, cyclic voltammetry, and electrochemical impedance spectroscopy. As shown in **Figure 3**a, S7a and S7b, the three anodes display similar charge-discharge profiles, in which the first cycle curve has a discharge-charge plateau at 0.14 and 1.2 V, respectively. In the following cycles, the discharge-charge plateau of three samples shift to 0.46 and 1.2 V, respectively, confirming similar lithiation/delithiation processes of the three ZIFs anodes. Highly stable cycling performance of electrodes plays an important role in the practical application of rechargeable batteries. In this regard, the cycling performances of the three above-mentioned anodes are evaluated at 2 A g^{-1} (Figure 3b), as well as at 0.1 and 0.5 A g^{-1} (Figure S7c and S7d). At 0.5 A g^{-1}, the discharge capacity (670 mA h g^{-1} ~ 5.2Li/formula unit) of the ZIF glass is significantly higher than those of other two samples (220 mA h g^{-1} ~ 1.7Li/formula unit for ZIF crystal and 125 mA h g^{-1} ~ 1.0Li/formula unit for amorphous ZIF) at the first cycle. However, the capacity of the ZIF glass decays to about 200 mA h g^{-1} after 20 cycles and remains unchanged till 100 cycles. This capacity is higher than those of both the ZIF crystal (149 mA h g^{-1}) and amorphous ZIF (125 mA h g^{-1}) (also see Figure S7d). In Figure 3b, an unusual phenomenon could be observed, that is, these three samples display continuous increases of the capacity during 1000 cycles at 2 A g^{-1}, respectively. Specifically, the capacities of ZIF crystal, ZIF glass and amorphous ZIF have reached 157, 188 and 306 mA h g^{-1} (~ 1.2, 1.5 and 2.4Li/formula unit), respectively, at the end of 1000 cycles. It is clearly seen that, compared with ZIF crystal and amorphous ZIF, the ZIF glass shows a more extensive enhancement in capacity after 1000 cycles, i.e., its capacity is tripled relative to the initial value of 95 mAh g^{-1} (Figure 3b). The increasing trend could be seen until 1500 cycles, after which the capacity

gradually decays (Figure S7e). Under the same condition, both ZIF crystal and amorphous ZIF exhibit the capacity enhancement, but to a lesser extent compared with ZIF glass anode (Figure S7f). When comparing the cycling curves between the amorphous ZIF and ZIF crystal, it is evident that the former shows slightly higher capacity than the latter. As shown in Figure 3c, the rate capacities of the three samples are determined at the current densities of 0.1, 0.5, 0.8 and 1 A g^{-1}, at each of which 20 cycles of discharging/charging are conducted. It is clearly seen that the capacity drops with increasing the current density. Remarkably, when the current density is switched back to 0.1 A g^{-1}, the capacities fully recover to the values corresponding to this current density for all the three samples.

To further evaluate the electrochemical performances of the three ZIF anodes, cyclic voltammetry (CV) measurements during the range from 0.01 to 3 V at a scan rate of 0.1 mV s^{-1} were conducted. As shown in Figure 3d, the CV curves of ZIF glass present the reduction peaks at 0.7 and 0.14 V in the first cathodic scan, and these peaks might originate from insertion of Li^+ ions into ZIF and formation of solid electrolyte interface film (SEI).[31] The peak at 1.2 V in the anodic scan is ascribed to the extraction of Li^+ ions from ZIF glass. In the subsequent two cycles, one couple of redox peaks (0.46/1.2 V) remain almost unchanged, corresponding to the reversible insertion/extraction of Li^+ ions into/from ZIF glass. As displayed in Figures 3d and S8, the redox peaks of the three samples occur at almost the same potential. This further confirms that three ZIF samples undergo an identical lithium storage process despite their structural difference. In addition, we studied the contributions of both the diffusion-controlled processes and the capacitive effects to the current by collecting CV curves of the three ZIF anodes at different scan rates. In other words, the kinetic analyses of the three ZIF samples were performed to determine whether the lithium storage in these materials is diffusion-limited or surface-controlled (capacitive). In Figures S9-11, it is revealed that the lithium ions diffusion-controlled mechanism predominates in ZIF glass and amorphous ZIF anodes during the discharge/charge process. In contrast, the current in ZIF crystal mostly arises from a capacitive

process. Therefore, it draws the conclusion that the highly enhanced capacity of ZIF glass anode might be closely related to the diffusion-controlled Li^+ insertion mechanism.

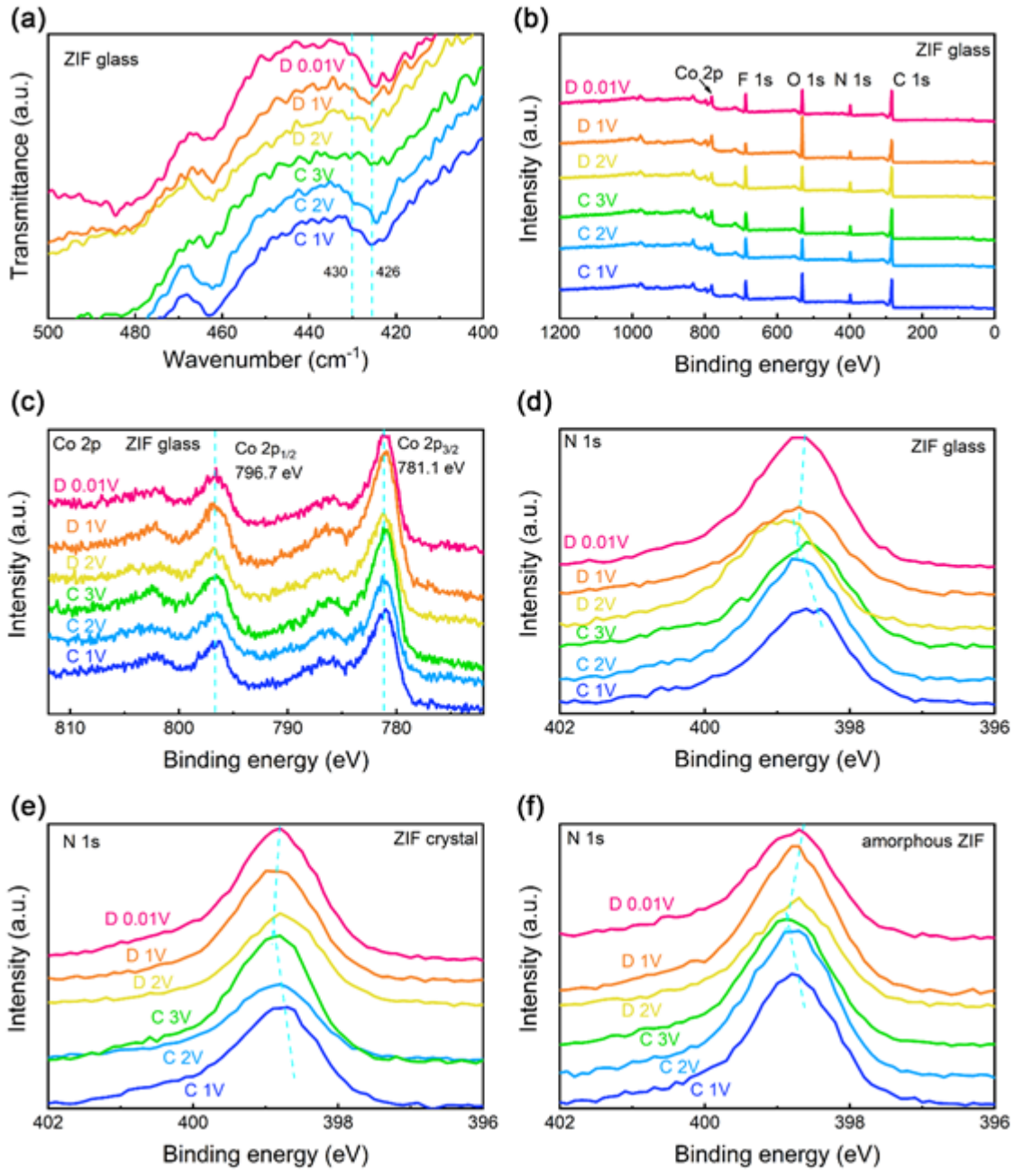

Figure 4. Ex situ spectroscopic characterization of ZIF crystal, ZIF glass and amorphous ZIF when they were charged to 1 V, 2 V, 3 V and then discharged to 2 V, 1 V and 0.01 V, which are denoted as C 1V, C 2V, C 3V, D 2V, D 1V and D 0.01V, respectively. (a) Ex situ FTIR spectra, (b) Ex situ XPS survey

spectra and (c) the high-resolution spectra of Co 2p for ZIF glass, the high-resolution spectra of N 1s for (d) ZIF glass, (e) ZIF crystal and (f) amorphous ZIF, respectively.

To observe the difference in electrical resistance among the three ZIF anodes, electrochemical impedance spectroscopy measurements were conducted as shown in Figure 3e. It is seen that the Nyquist plots of the three anodes consist of a depressed semicircle in high frequency range and a straight line at low frequency end. The equivalent circuit model of the experimental curves is shown in Figure S12. The R_b (bulk resistance of the cell) of ZIF crystal, ZIF glass and amorphous ZIF are found to be 2.68, 4.95 and 3.57 Ω, respectively (Table S2). The R_{ct} (charge transfer resistance) of the amorphous ZIF is the smallest (52 Ω) among the three samples, indicating the highest electrical conductivity. The low-frequency sloping line is ascribed to the Warburg impedance, which is associated with the diffusion of Li^+ ions in the electrode material. Thus, the apparent Li^+ ion diffusion coefficient *D* of three ZIF samples are calculated from the incline line in the Warburg region using equation:[32]

$$D=R^2T^2/2A^2n^4F^4C^2\sigma^2 \quad (1)$$

where *R* is the gas constant, *T* is the absolute room temperature, *A* is the surface area of the electrode (~1.13 cm^2), *n* is the number of electron transferred during oxidation, *F* is the Faraday constant, *C* is the Li^+ concentration, and σ is the Warburg factor associated with Z_{re} ($Z_{re} \propto \sigma\omega^{-1/2}$). σ can be determined from the linear relation between Z_{re} and the reciprocal square root of the angular frequency ω (Figure 3f). By introducing σ into Equation (1), we can calculate the apparent Li^+ diffusion coefficient *D* since the temperature and other constants are known. Thus, the *D* values of ZIF crystal, ZIF glass and amorphous ZIF are found to be 2.82×10^{-14}, 1.06×10^{-14} and 0.65×10^{-14} cm^2 s^{-1}, respectively. As for ZIF samples after 1000 cycles (Figure S13), they exhibit the similar CV curves with two oxidation peaks (1.4 V and 1.94 V) and two reduction peaks (1.68 V and 0.93 V), suggesting

the same lithium storage mechanism. In addition, the apparent Li^+ diffusion coefficient *D* for ZIF crystal, ZIF glass and amorphous ZIF after 1000 cycles are determined to be 9.14×10^{-13}, 3.50×10^{-13} and 2.10×10^{-12} cm^2 s^{-1}, respectively.

Ex situ FTIR of the three ZIF samples were collected to study the structural evolution during charge-discharge process (**Figure 4**a and S14). In Figure 4a, the band at around 426 cm^{-1} of ZIF glass remains almost unchanged during one charge-discharge cycle, indicating that the lithiation/delithiation process has little impact on Co-N bond of the ZIF. In order to explore the microstructural roots in the different electrochemical performances among the three samples, ex situ XPS measurements were conducted on the anodes which were charged to 1, 2, 3 V and then discharged to 2, 1, 0.01 V, respectively (Figures 4b-4f, S15-17). In Figures 4b, S15, S16a and S16c, it is clearly seen that F and O are present in all three samples, which originate from the SEI film. To investigate the effect of cycling process on the valence state of cobalt, the Co 2p spectra of the three ZIF samples at different charge/discharge potential were also collected (Figures 4c, S16b and S16d). Two peaks at 796.2 eV (Co $2p_{1/2}$) and 780.8 eV (Co $2p_{3/2}$) indicate the existence of Co^{2+}, as well as two satellite peaks were detected in each spectrum, which are significant different from those of metallic Co (793.3 eV for Co $2p_{1/2}$ and 778.0 eV for Co $2p_{3/2}$). This suggests that the valence state of Co is not influenced by charge-discharge processes for all three ZIF samples. In addition, the high-resolution spectra of C 1s and N 1s also remain unchanged upon cycling as evidenced in Figures 4d-4f and S17. In C 1s spectra of ZIF samples after 1000 cycles, the peaks at around 284 eV originate from CO_3^{2-} in SEI layer (Figure S17). All XPS results (Figures. 4, S16 and S17) suggest that both the metal nodes and organic ligands in all ZIF samples remain unaltered during the charge-discharge process. Interestingly, the N 1s peaks of all three ZIF samples shift to higher binding energy upon delithiation process and gradually recover upon lithiation (Figure 4d-f). The variation of the peak position upon lithiation/delithiation could be ascribed to the chemical interactions between nitrogen atoms from ligands and lithium. In

addition, the recovery of the peak position implies the outstanding reversibility and cycling stability of the three ZIF anodes.

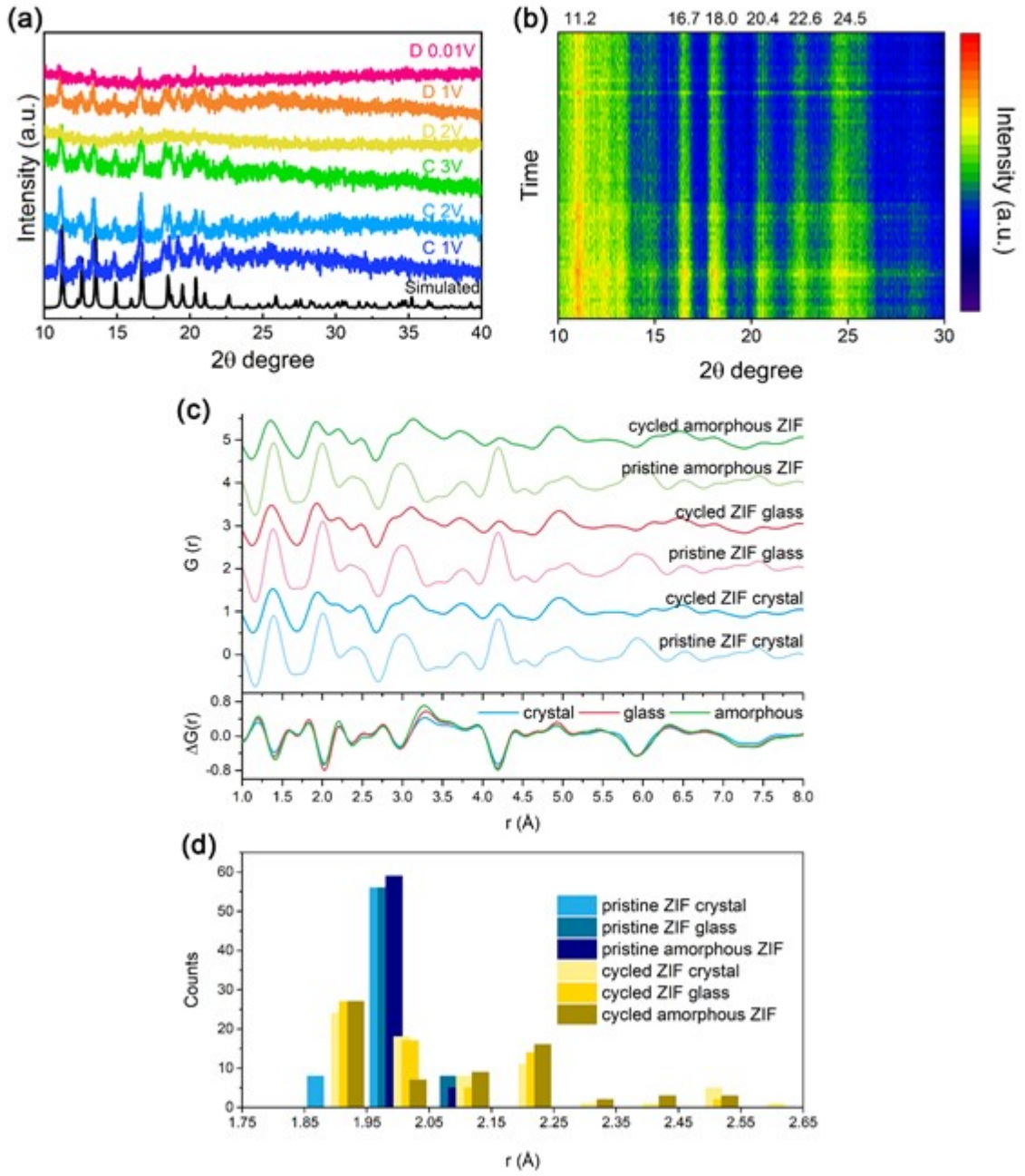

Figure 5. Ex and in situ XRD patterns of ZIF crystal and PDF analysis of the ZIF anodes prior to and after 1000 charge-discharge cycles. (a) Ex situ XRD patterns of ZIF crystal. The ZIF crystal electrode were charged in coin cells to 1 V, 2 V, 3 V and then discharged to 2 V, 1 V and 0.01 V, respectively. (b) In situ XRD patterns of ZIF crystal. The ZIF crystal was mixed with binder (PTFE) and the XRD

patterns were collected from as-prepared electrode during the range from 10 to 30 degree during the 2nd cycle to 7th cycle. (c) Comparison of PDFs for the pristine and cycled anodes and the difference PDF, i.e. ($\Delta G(r) = G(r)_{cycled\text{-}anode} - G(r)_{pristine\text{-}anode}$. (d) Number of nearest Co-N coordination distances within ranges of 0.1 Å in the pristine and cycled ZIF anodes.

To explore the structural evolution of ZIF crystal upon discharge/charge cycles, ex situ and in situ XRD patterns were collected. **Figure 5**a shows the ex situ XRD patterns of ZIF crystal after the first cycle. The angular positions of the characteristic diffraction peaks of the ZIF crystal show no significant changes upon the second lithiation-delithiation process, however, the overall diffraction peak intensity decreases during the process suggesting some loss of crystallinity. To verify this, in situ XRD patterns of the ZIF crystal anode from the 2nd to 7th cycle were also obtained (Figure 5b). Both the angular position and relative intensity of the diffraction peaks keep almost unchanged. This indicates that the crystal structure remains stable during the first several discharge/charge cycles, however, the ex situ XRD confirms that some crystallinity is lost during cycling. This is corroborated by the complete loss of diffraction peaks (Figure S18) in the XRD patterns of the ZIF crystal anode after 1000 cycles. This implies that that the structural changes of ZIF crystal are subtle during each cycle and that the resulting structural evolution in ZIF crystal after 1000 cycles from crystal to amorphous state is a cumulative effect of each discharge/charge cycles, which could be the main reason for the progressively increased capacity upon cycles (Figure 3b).

To further investigate the origin of the cycling-induced capacity enhancement, PDFs of the three ZIF anodes were obtained from total X-ray scattering data collected from anodes prior to cycling (pristine) and after 1000 charge-discharge cycles (Figure 5c). Firstly, it is evident that the local structures of the three cycled ZIF anodes are highly similar. Secondly, comparing the difference PDF ($\Delta G(r) = G(r)_{cycled\text{-}anode} - G(r)_{pristine\text{-}anode}$), it is clear that the structural change induced by the continued

charge-discharge process is almost identical in the three ZIF anodes. Thirdly, it is noticed that cycling causes significant loss of long-range order even for the already disordered glassy and amorphous ZIFs (e.g., loss of correlations at ~4.2 and 6.0 Å), and no well-defined correlations are observed >5 Å. Notice that in the structure of Co-ZIF-62 only a few intermolecular distances are <5 Å, and these are all found around the $[CoN_4]$-tetrahedra. Hence, the correlations in the observed PDFs after cycling can be assigned to intramolecular distances and the short Co-N and Co-C distances. Comparing the observed correlations in the PDFs to the structural model for crystalline Co ZIF-62 (Figure S19) suggests that the main differences at the local scale (<5 Å) are related to correlations involving Co, which is consistent with the assumption that the strong covalent bonds in the imidazole and benzimidazole keeps the molecules intact. Hence, to obtain quantitative insight into the local structures (<4.5 Å) of the anodes, the positions of the 16 Co atoms in the unit cell were refined independently without symmetry constraints (see fits in Figure S20 and refined parameters in Table S3). This revealed a much wider distributions of Co-N coordination distances in the $[CoN_4]$-tetrahedra after cycling (Figure 5d). In the pristine electrodes, the Co-N distances are in the range 1.85-2.05 Å for ZIF crystal and 1.95-2.15 Å for ZIF glass and amorphous ZIF. After cycling, ca. half the Co-N distances increases significantly. While most of the Co-N distances in the cycled anodes fall in the range 1.85-2.25 Å, ca. 15% are >2.25 Å and some up to 2.65 Å. These distances are so long that the Co-N coordination may be considered broken. Hence, repeated charge-discharge cycling causes distortion of the local Co-N coordination environment and eventually breakage of some of the Co-N coordinations. The breakage of Co-N coordinations may “open” the Co ZIF-62 structure for more efficient Li-intercalation, by making new Li-diffusion pathways available and make some of the Li-sites more accessible. Hence, this may explain the cycling induced capacity increase.

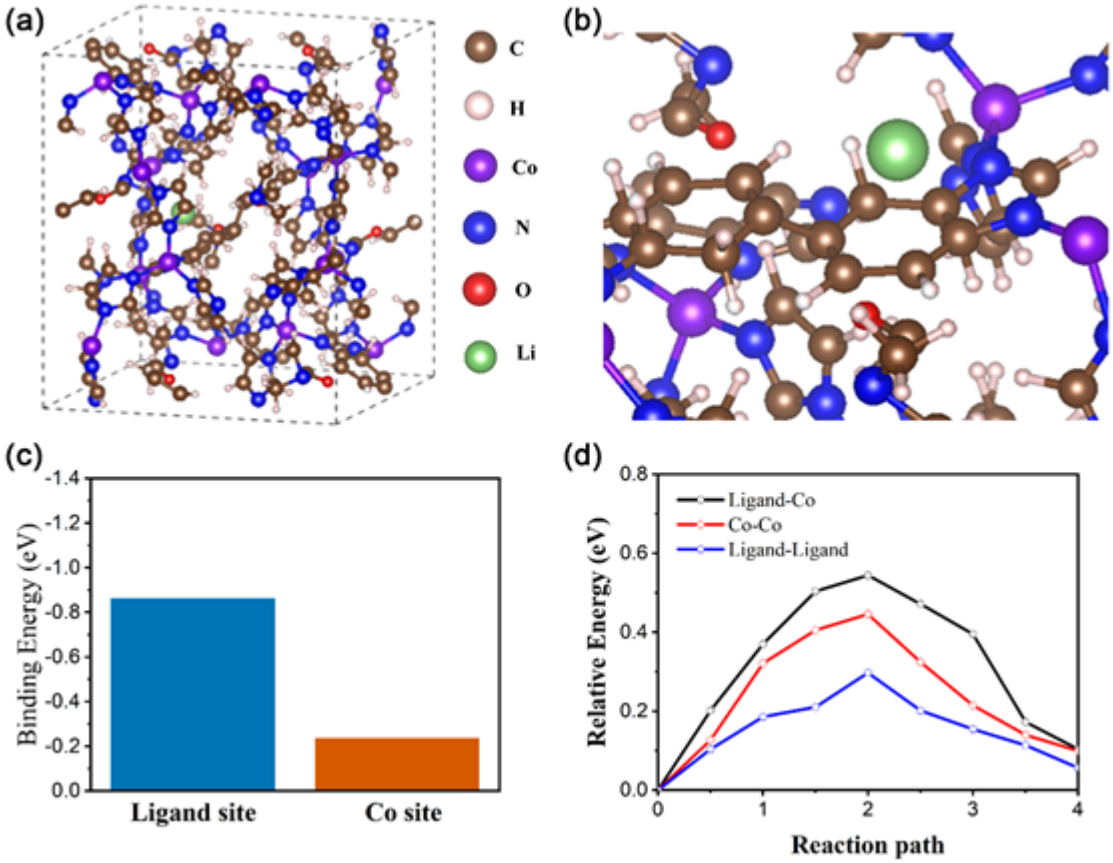

Figure 6. DFT calculation of binding sites, binding energy, and reaction path for Li^+ ions. (a) The simulated structure of ZIF crystal and lithium binding sites (organic ligands, which is noted as ligand site). (b) Enlarged figure of lithium binding site (aromatic ring from organic ligand) in ZIF crystal. (c) The binding energy of ligand site and metal site. (d) Relative energy barriers of different diffusion paths (from ligand to Co node, Co node to Co node, and ligand to ligand).

To probe the lithium storage dynamics, the energy for lithium ions bonded to different site and the lithium-ion diffusion energy barriers of different trajectories in ZIF crystal were determined by density functional theory (DFT) calculations (**Figure 6**). The results reveal that the aromatic rings in the organic ligands (imidazole and benzimidazole) act as binding site for lithium ions storage due to the higher binding energy of -0.86 eV (Figures 6a-6c, S21-23) compared to other sites, e.g., Co

coordinate (the calculated binding energy of -0.24 eV). In addition, nitrogen atoms in the ligands could also act as active sites to react with lithium ions according to a previous study,[33] which contribute a theoretical capacity about 600 mAh g^{-1}. These results further confirm the unchanged valance state of Co during the lithiation-delithiation process, being consistent with the XPS results. As presented in Figures 6d and S22, the energy barrier for Li^+ ion diffusion from ligand to ligand is much lower than those from ligand to Co node and from Co node to Co node. Moreover, the small volume change (ΔV~0.3%) in ZIF crystal occurring during the lithiation process (Table S4) might be related to the large pore size of ZIF crystal, agreeing with in situ XRD results (Figure 5b). In addition, the reaction between organic ligands and Li^+ ions might weaken the coordination bond (e.g., Co-N), leading to bond distortion or breakage. While the overall skeleton of ZIF is preserved after cycling, confirmed by their PDFs as well as SEM and TEM images (Figure S24), the ZIF crystal experience an order-disorder transition and lost its long-range order during repeating charge-discharge processes.[11] In detail, some weak coordination bonds between cobalt nodes and organic ligands could be easily broken during lithiation/delithiation, and thus the tetrahedral $Co(Im/bIm)_4$ network is partially depolymerized. This leads to the formation of larger channels (compared to the pristine ones), and hence, facilitating both the Li^+ ions diffusion and storage. The lithium storage mechanism of both the ZIF glass and amorphous ZIF is same as that of ZIF crystal, i.e., the lithium storage mainly originates from the organic parts of ZIF. These three materials experience the same structural evolution.

The remarkable cycling-induced enhancement of capacity in the ZIF glass anode is associated with the disordered open network structure. In detail, such structure possesses three striking features as follows. First, it is disordered at all the length scales such as short-range (0.5-0.8 nm), medium-range (0.8-2 nm) and long-range (>20 nm),[16,21] in contrast to other types of network glasses (e.g., oxide glasses). Second, the connection between metal nodes and ligands is established by the coordination bonds, which are much weaker than the covalent and ionic bonds in inorganic glasses. Third, ZIF

glass structure is also in highly metastable state with higher potential energy compared to ZIF crystal, suggested by the red shift of Co-N bond from FTIR spectra. These three features make ZIF glass more easily affected by Li^+ ion insertion and extraction under high current density, so that the number and size of the transfer channels for Li^+ ions would increase with cycling, and hence the capacity would be enhanced.

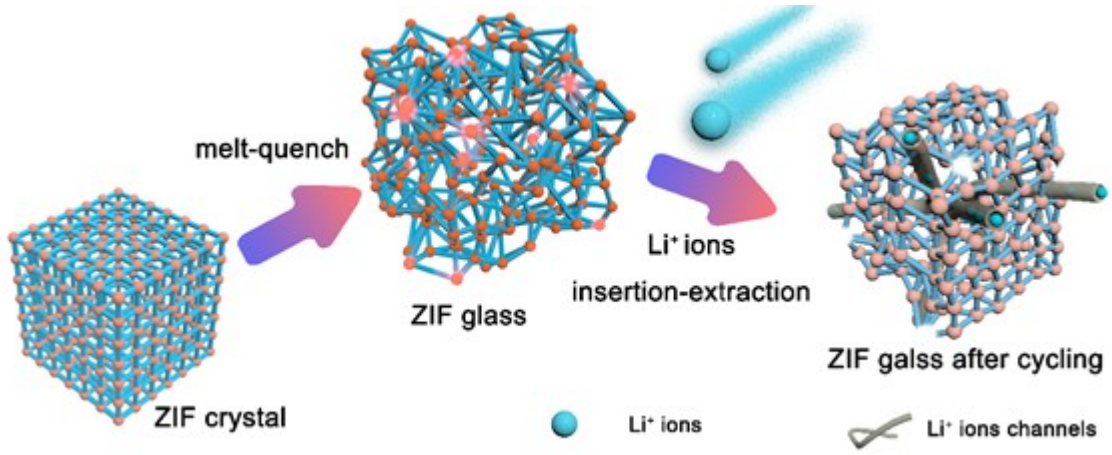

However, due to the more stable structure, both the degree of the network depolymerization and the structural defect concentrations in ZIF crystal are much lower than ZIF glass and amorphous ZIF, and therefore its capacity enhancement during cycling is the lowest among three ZIF samples. Different from ZIF crystal, amorphous ZIF contains numerous structural defects such as broken bonds, unsaturated coordination for both nodes and ligands and vacancies, which are induced by mechanical impact during the ball milling process. These defects act as active sites for Li^+ ion storage and transfer. These defects also weaken the ZIF network, so that the Li^+ insertion/extraction can depolymerize the network, and thereby new channels are created. Therefore, the capacity of the amorphous ZIF anode is enhanced during cycling.

Scheme 1. The schematic representation of the structural origin of the capacity enhancement in ZIF glass anode.

Based on the above discussions, the mechanism of the cycling-induced capacity enhancement in ZIF glass anode may be schematically illustrated in **Scheme 1**. Upon heating, ZIF crystal is melted, and thereby its network structure becomes disordered at all length scales (short-, medium- and long-range).[16,21] Upon quenching, the disordered structure is frozen-in in the glass state with higher potential energy (compared with crystal state). Once the Li^+ ions insert into the network structure, they will affect and disrupt the coordination bonds, leading to the distortion and local breakage of the Co-N coordination, and hence, generating new channels for Li^+ ion diffusion and storage. Consequently, the capacity of the glass anode substantially increases with cycling. Moreover, the short-range disorder in ZIF glass structure enables shortening the diffusion distance of Li^+ ions, benefiting the ionic transfer kinetics. In addition, the high-energy state of ZIF glass makes the network structure easily be distorted and depolymerized by insertion/extraction of Li^+ ions during charge-discharge cycles, and this favors the formation of new channels for Li^+ ion diffusion and storage. Thus, this type of ZIF glass (i.e., melt-quench Cobalt-ZIF-62 glass) exhibit great potential as a promising anode material for fabricating superior Li ion batteries.

4. Conclusions

The MOF glass anode has been developed for Li-ion batteries, which is based on the Cobalt-ZIF-62, i.e., $Co[Im_{1.75}bIm_{0.25}]$. This novel type of anode exhibits unusual lithium storage performances such as larger capacity, better rate capability and higher cycling stability, compared with crystalline and amorphous counterparts, although these materials have the same chemical composition. The distinctive performances were attributed to the open network structure characterized by a high degree of disorder at all scales and higher energy state. Extraordinarily, the ZIF glass anode exhibits a tripled increase of the specific capacity (up to 306 mA h g^{-1}) after 1000 cycles at the current density

of 2 A g^{-1}. The origin of this remarkable phenomenon has been revealed by performing spectroscopic measurements, pair distribution function analyses and density functional theory calculations. Specifically, the insertion and extraction of Li^+ ions into the ZIF network structure disrupts and breaks the Co-N coordination bonds, and thereby generates additional channels for Li^+ ion diffusion and storage. These findings indicate that MOF glasses are the promising materials for developing the next generation of anodes for high performance Li^+ ion batteries.

5. Methods

Synthesis of ZIF crystal, ZIF glass and amorphous ZIF

Crystalline ZIF-62 (Co) was synthesized by a modified method based on previously literatures.[19,22,24,34,35] In detail, imidazole (Im, 11.55 mmol, 785.4 mg) and benzimidazole (BIm, 1.66 mmol, 196 mg) were dissolved in 90 mL *N,N*-dimethylformamide (DMF). Then, $Co(NO_3)_2{\cdot}6H_2O$ (4 mmol, 1164 mg) was dissolved in above solution. After stirring for 0.5 h, the solution was transferred into an oven and heated at 130 ℃for 3 days. After cooling, the purple product was separated by centrifugation and dried under vacuum at 120 ℃ overnight. To obtain melt-quenched ZIF glass, the finely ground crystalline ZIF-62 was heated at 10 ℃ min^{-1} to 450 ℃ and calcined at this temperature for 5 minutes followed by cooling naturally to room temperature. The whole process was purged with argon. The mechanical amorphous ZIF-62 was prepared by ball milling the crystalline sample at 500 rpm for 10 h. For simplicity, these samples (ZIF-62 (Co) crystal, melt-quenched ZIF and mechanical ball milling amorphous ZIF) are denoted as ZIF crystal, ZIF glass and amorphous ZIF, respectively.

Material Characterizations

Powder X-ray diffraction (XRD) measurements of the samples were performed on a PANalytical X-ray diffractometer with Cu Kα (λ = 1.5406 Å) radiation during the 2θ range of 10-60° with a step size of 0.013°. Ex situ XRD of ZIF crystal were collected when they were charged to 1 V, 2 V, 3 V and then discharged to 2 V, 1 V and 0.01 V, respectively. Then, these coin cells were opened, and the samples were taken out for XRD measurement in the range from 10 to 40 degree. In situ XRD patterns were obtained by mixing ZIF crystal with PTFE as the binder, then collected from 10 to 30 degree. Synchrotron XRD and X-ray total scattering measurements were performed for the as-prepared materials (i.e., ZIF crystal, ZIF glass and amorphous ZIF), the as-prepared electrodes of the three materials and of electrodes of the three materials after 1000 charge-discharge cycles. These measurements were performed at beamline 11-ID-B at the Advanced Photon Source, Argonne National Laboratory, Chicago, USA. The hard X-ray wavelength was 0.2115 Å. The samples were contained inside kapton (polyimide) capillaries (1.0 mm inner diameter, Cole-Parmer) and the data was collected using a PerkinElmer XRD1621 area detector. For detector calibration, a cerium dioxide, CeO_2, standard (NIST 674b) was used. Exposure times of 30 s and 5 min were used for the XRD and total scattering data collection, respectively. The collected two-dimensional scattering patterns were masked and azimuthally integrated into one-dimensional diffractograms using the Fit2D software.[36] To obtain PDFs, the total scattering data was Fourier transformed using the PDFgetX3 software.[37] The instrumental maximum Q-value, was set to 23.5 $Å^{-1}$ and that of Q_{min} was set to 0.1 $Å^{-1}$. The value of r_{poly} was set to 1.35.

PDFs for all samples were refined using the software TOPAS Academic.[38] In all cases the crystalline model for Cobalt-ZIF-62 (CCDC No. 671070) was used as starting model. For the PDFs refinements a Q_{damp} of 0.069 was used (obtained from refinement of a PDF for a CeO_2 NIST standard). Generally, cell parameters (*a*, *b* and *c*), spherical diameter (sp-diameter), fractional coordinates of Co and thermal vibration factors for each atom type except H were refined. The *r*-dependence of the thermal vibration factors was accounted for with a simple r_{cut} function (see Tables S1 and S3).

Specifically, for local structure refinements (*r*-range: 1.0 - 4.5 Å) the structural Co ZIF-62 model was expanded from *Pbca* to *P*1 symmetry giving rise to 416 atoms in the unit cell. All unit cell parameters, all 16 Co-positions and the isotropic vibration factor >4.7 Å of Co were refined. We note that the positions and orientations of the imidazole and benzimidazole molecules likely also changes somewhat during the 1000 charge-discharge cycles. However, the PDFs do not provide statistically significant insight into intermolecular distances and the relative positions of the molecules cannot be determined.

The thermal properties of samples were determined by the differential scanning calorimetry (DSC) (STA 404C Netzsch) in N_2 atmosphere at a heating rate of 10 °C min^{-1}. Mass losses of samples with temperature were obtained simultaneously to the DSC scan by thermogravimetry (TG). The Raman spectroscopy measurements were conducted via Renishaw In-Via Raman microscopic with an Ar^+ laser (λ = 785 nm) at 50 × aperture. Fourier transform infrared (FTIR) spectra were recorded on a Bruker TENSOR II FTIR spectrometer with Platinum ATR Accessory at room temperature in the range of 400-4000 cm^{-1}. X-ray photoelectron spectroscopy (XPS) was performed by using ESCALAB 250Xi spectrometer (ThermoFisher Scientific, USA) with non-monochromatic Al Ka X-ray (1486.6 eV) at pass energy of 50 eV to determine the surface properties and chemical compositions of the samples. N_2 adsorption-desorption isotherms were collected at 77 K with an ASAP 2020 Accelerated Surface Area and Porosimetry System; Brunauer-Emmett-Teller (BET) and Barrett-Joyner-Halenda (BJH) analyses were performed to calculate the specific surface area, and the corresponding pore size distribution. CO_2 gas physisorption measurements were conducted at 273 K with a Micromeritics ASAP 2460 instrument using CO_2 gas of 99.995% purity. A thermostat was used for the sample environment. Samples have been evacuated at high vacuum and 200 °C for 2 h prior to data collection.

Cell assembly and Electrochemical Characterizations

All electrochemical measurements were repeated with different batches of three ZIF samples to confirm the reproducibility of their performance. The electrochemical performance of the as-prepared ZIF crystal, ZIF glass and amorphous ZIF were evaluated by coin-type cell CR2032 with metallic lithium foil (diameter of 16.0 mm) as the counter electrode. The electrolyte consists of 1 M $LiPF_6$ in ethylene carbonate (EC)/diethyl carbonate (DEC)/dimethyl carbonate (DMC) (1:1:1 vol%) and a Celgard 2325 membrane (diameter of 19.0 mm) functions as the separator. The working electrodes consist of the active powder materials (70 wt %), conductive acetylene black (20 wt %) as a conductor, and polyvinylidene difluoride (PVDF) (10 wt %) as a binder. All the components were mixed well to form a slurry and pasted onto copper foil substrate. After being dried at 110 °C in a vacuum oven for 12 h, the foil was cut into circular electrode with a diameter of 12 mm. The loading mass of active materials is 1-2 mg, based on which the gravimetric capacity was calculated. The cells were assembled in an Argon-filled glovebox with both the moisture and the oxygen content below 1 ppm and tested at 25 °C. The galvanostatic charge/discharge tests of the cells were carried out on a Land battery test system (CT2001A). Cyclic voltammetry (CV) curves were recorded in the voltage range of 0.01-3 V at the scanning rate of 0.1 mV s^{-1} and EIS spectra were obtained in the frequency range of 0.1 to 100 kHz on a CHI 760e electrochemical workstation with an amplitude of 5 mV.

Computational methods

The Vienna Ab Initio Package (VASP)[39,40] was employed to perform all the density functional theory (DFT) calculations within the generalized gradient approximation (GGA) using the PBE formulation.[41] The projected augmented wave (PAW) potentials[42,43] was chosen to describe the ionic cores and take valence electrons into account using a plane wave basis set with a kinetic energy cutoff of 450 eV. Partial occupancies of the Kohn−Sham orbitals were allowed using the Gaussian smearing method and a width of 0.05 eV. The electronic energy was considered self-consistent when the energy change was smaller than 10^{-5} eV. A geometry optimization was considered convergent

when the force change was smaller than 0.03 eV/Å. Grimme's DFT-D3 methodology was used to describe the dispersion interactions.[44] A 2×2×2 Monkhorst-Pack k-point grid for Brillouin zone sampling for structure. Finally, the Binding energies (E_b) are calculated as $E_b = E_{ad/sub} - E_{ad} - E_{sub}$, where $E_{ad/sub}$, E_{ad} and E_{sub} are the optimized adsorbate/substrate system, the adsorbate in the structure and the clean substrate respectively. And the migration barrier had been calculated using the climbing Image-Nudged Elastic Band methods.

Supporting Information

Supporting Information is available from the Wiley Online Library or from the author.

Acknowledgements

This work was financially supported by the China Scholarship Council (201707040085), the Taishan Young Scholarship Project of Shandong Province (tsqn202103098), the Shandong Provincial Natural Science Foundation (ZR2020ME025), the Colleges and Universities Twenty Terms Foundation of Jinan City (2019GXRC034) and Foundation from State Key Laboratory of Special Glass of China. C. Gao would like to thank Jiajia Yan, Pengfei Liu, Ang Qiao, Fangyu Xiong for their great help in data collection. This research used resources of the Advanced Photon Source, a U.S. Department of Energy (DOE) Office of Science User Facility operated for the DOE Office of Science by Argonne National Laboratory under Contract No. DE-AC02-06CH11357.

Received: ((will be filled in by the editorial staff))
Revised: ((will be filled in by the editorial staff))
Published online: ((will be filled in by the editorial staff))

Conflict of Interest

The authors declare no conflict of interest.

References

[1] C. K. Chan, H. Peng, G. Liu, K. McIlwrath, X. F. Zhang, R. A. Huggins, Y. Cui, *Nat. Nanotechnol.* **2008**, *3*, 31.

[2] J.-M. Tarascon, M. Armand, *Nature* **2001**, *414*, 359.

[3] G. N. Zhu, Y. G. Wang, Y. Y. Xia, *Energy Environ. Sci.* **2012**, *5*, 6652.

[4] L. Wang, Y. Han, X. Feng, J. Zhou, P. Qi, B. Wang, *Coord. Chem. Rev.* **2016**, *307*, 361.

[5] S. Maiti, A. Pramanik, U. Manju, S. Mahanty, *ACS Appl. Mater. Interfaces* **2015**, *7*, 16357.

[6] L. Chen, W. Yang, J. Wang, C. Chen, M. Wei, *Chem. - Eur. J.* **2018**, *24*, 13362.

[7] X. Li, F. Cheng, S. Zhang, J. Chen, *J. Power Sources* **2006**, *160*, 542.

[8] H. Yue, Z. Shi, Q. Wang, Z. Cao, H. Dong, Y. Qiao, Y. Yin, S. Yang, *ACS Appl. Mater. Interfaces* **2014**, *6*, 17067.

[9] A. Banerjee, U. Singh, V. Aravindan, M. Srinivasan, S. Ogale, *Nano Energy* **2013**, *2*, 1158.

[10] W. Chaikittisilp, K. Ariga, Y. Yamauchi, *J. Mater. Chem. A* **2013**, *1*, 14.

[11] C. Gao, P. Wang, Z. Wang, S. K. Kær, Y. Zhang, Y. Yue, *Nano Energy* **2019**, *65*, 104032.

[12] T. D. Bennett, S. Cao, J. C. Tan, D. A. Keen, E. G. Bithell, P. J. Beldon, T. Friscic, A. K. Cheetham, *J. Am. Chem. Soc.* **2011**, *133*, 14546.

[13] Y. Ohara, A. Hinokimoto, W. Chen, T. Kitao, Y. Nishiyama, Y. Hong, S. Kitagawa, S. Horike, *Chem. Commun.* **2018**, *54*, 6859.

[14] T. D. Bennett, D. A. Keen, J. C. Tan, E. R. Barney, A. L. Goodwin, A. K. Cheetham, *Angew. Chem., Int. Ed.* **2011**, *50*, 3067.

[15] K. W. Chapman, G. J. Halder, P. J. Chupas, *J. Am. Chem. Soc.* **2009**, *131*, 17546.

[16] T. D. Bennett, J. C. Tan, Y. Yue, E. Baxter, C. Ducati, N. J. Terrill, H. H. M. Yeung, Z. Zhou, W. Chen, S. Henke, A. K. Cheetham, G. N. Greaves, *Nat. Commun.* **2015**, *6*, 1.

[17] T. D. Bennett, Y. Yue, P. Li, A. Qiao, H. Tao, N. G. Greaves, T. Richards, G. I. Lampronti, S. A. T. Redfern, F. Blanc, O. K. Farha, J. T. Hupp, A. K. Cheetham, D. A. Keen, *J. Am. Chem. Soc.* **2016**, *138*, 3484.

[18] S. S. Sørensen, M. B. Østergaard, M. Stepniewska, H. Johra, Y. Yue, M. M. Smedskjaer, *ACS Appl. Mater. Interfaces* **2020**, *12*, 18893.

[19] A. Qiao, T. D. Bennett, H. Tao, A. A. Krajnc, G. Mali, C. M. Doherty, A. W. Thornton, J. C. Mauro, G. N. Greaves, Y. Yue, *Sci. Adv* **2018**, *4*, 1.

[20] M. Stepniewska, K. Januchta, C. Zhou, A. Qiao, M. M. Smedskjaer, Y. Yue, *Proc. Natl. Acad. Sci. U. S. A.* **2020**, *117*, 10149.

[21] R. S. K. K. Madsen, A. Qiao, J. Sen, I. Hung, K. Chen, Z. Gan, S. Sen, Y. Yue, *Science* **2020**, *367*, 1473.

[22] L. Frentzel-Beyme, M. Kloß, R. Pallach, S. Salamon, H. Moldenhauer, J. Landers, H. Wende, J. Debus, S. Henke, *J. Mater. Chem. A* **2019**, *7*, 985.

[23] L. Frentzel-Beyme, M. Kloß, P. Kolodzeiski, R. Pallach, S. Henke, *J. Am. Chem. Soc.* **2019**, *141*, 12362.

[24] R. Banerjee, A. Phan, B. Wang, C. Knobler, H. Furukawa, M. O'Keeffe, O. M. Yaghi, *Science* **2008**, *319*, 939.

[25] Q. Zheng, Y. Zhang, M. Montazerian, O. Gulbiten, J. C. Mauro, E. D. Zanotto, Y. Yue, *Chem. Rev* **2019**, *119*, 7848.

[26] C. P. Wong, P. J. Miller, *J. Energ. Mater.* **2005**, *23*, 169.

[27] A. Schneemann, V. Bon, I. Schwedler, I. Senkovska, S. Kaskel, R. A. Fischer, *Chem. Soc. Rev.* **2014**, *43*, 6062.

[28] S. Gadipelli, W. Travis, W. Zhou, Z. Guo, *Energy Environ. Sci.* **2014**, *7*, 2232.

[29] S. Yang, R. Lv, C. Wang, Y. Liu, Z. Song, *J. Alloys Compd.* **2013**, *579*, 628.

[30] C. Hu, Y. C. Huang, A. L. Chang, M. Nomura, *J. Colloid Interface Sci.* **2019**, *553*, 372.

[31] C. Li, X. Lou, Q. Yang, Y. Zou, B. Hu, *Chem. Eng. J.* **2017**, *326*, 1000.

[32] X. L. Wu, Y. G. Guo, J. Su, J. W. Xiong, Y. L. Zhang, L. J. Wan, *Adv. Energy Mater.* **2013**, *3*, 1155.

[33] Y. Lin, Q. Zhang, C. Zhao, H. Li, C. Kong, C. Shen, L. Chen, *Chem. Commun.* **2015**, *51*, 697.

[34] M. Gustafsson, X. Zou, *J. Porous Mater.* **2013**, *20*, 55.

[35] M. Stepniewska, M. B. Østergaard, C. Zhou, Y. Yue, *J. Non-Cryst. Solids* **2020**, *530*, 119806.

[36] A. Hammersley, "FIT2D: An Introduction and Overview," can be found under https://www.esrf.fr/computing/scientific/FIT2D/FIT2D_INTRO/fit2d.html, **1997**.

[37] P. Juhás, T. Davis, C. L. Farrow, S. J. L. Billinge, *J. Appl. Crystallogr.* **2013**, *46*, 560.

[38] A. A. Coelho, *J. Appl. Crystallogr.* **2018**, *51*, 210.

[39] G. Kresse, J. Furthmüller, *Phys. Rev. B* **1996**, *54*, 11169.

[40] J. P. Perdew, K. Burke, M. Ernzerhof, *Phys. Rev. Lett.* **1996**, *77*, 3865.

[41] G. Kresse, D. Joubert, *Phys. Rev. B* **1999**, *59*, 1758.

[42] P. E. Blöchl, *Phys. Rev. B* **1994**, *50*, 17953.

[43] S. Grimme, J. Antony, S. Ehrlich, H. Krieg, *J. Chem. Phys.* **2010**, *132*, 154104.

[44] G. Henkelman, B. P. Uberuaga, H. Jónsson, *J. Chem. Phys.* **2000**, *113*, 9901.

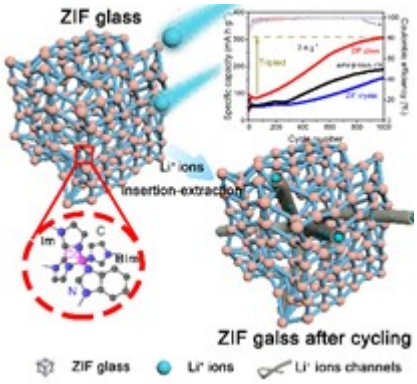

Metal-organic framework glass anode with an exceptional cycling-induced capacity enhancement for lithium-ion batteries

Chengwei Gao, Zhenjing Jiang, Shibin Qi, Peixing Wang, Lars Rosgaard Jensen, Morten Johansen, Christian Kolle Christensen, Yanfei Zhang*, Dorthe Bomholdt Ravnsbæk*, Yuanzheng Yue*

A ZIF glass (melt-quench Co ZIF-62 glass), for the first time, is evaluated as anode for high performance LIBs. This ZIF glass anode exhibits an unusual capacity enhancement along with cycling. This exceptional phenomenon is related to the unique structure of ZIF glass, i.e., high energy state, short range disorder.